Electronic Supplementary Information

Ruthenium Oxychloride Supported by Manganese Oxide for Stable Oxygen Evolution in Acidic Media†

Yunxing Zhao,‡[a] Jun Hu,‡[b] Chao-Lung Chiang,[c] Ying Li,[a] Weichuang Yang,[d] Zhenhai Yang,[d] Wei-Hsuan Hung,[e] Yan-Gu Lin,[c] Zhong Chen,[f] Bin Li,[a] Pingqi Gao*[a] and Hong Li*[ghi]

[a]School of Materials, Sun Yat-sen University, Guangzhou 510275, China. E-mail: gaopq3@mail.sysu.edu.cn

[b]School of Chemical Engineering, Northwest University, Xi'an 710069, China

[c]Scientific Research Division, National Synchrotron Radiation Research Center, Hsinchu 30076, Taiwan

[d]Ningbo Institute of Material Technology and Engineering, Chinese Academy of Sciences, Ningbo 315201, China

[e]Institute of Materials Science and Engineering, National Central University, Taoyuan 320317, Taiwan

[f]School of Materials Science and Engineering, Nanyang Technological University, 639798, Singapore.

[g]School of Mechanical and Aerospace Engineering, Nanyang Technological University, 639798, Singapore

[h]CINTRA CNRS/NTU/THALES, UMI 3288, Research Techno Plaza, 637553, Singapore

[i]Centre for Micro-/Nano-electronics (NOVITAS), School of Electrical and Electronic Engineering, Nanyang Technological University, 639798, Singapore. E-mail: ehongli@ntu.edu.sg

‡ Equal contribution.

1. Experimental Section

1.1 Material fabrication

All chemicals were used as received without further purification. $RuCl_3 \cdot xH_2O$ was purchased from Wokai Chemical Reagent Co. Ltd. RuO_2 was purchased from Sigma-Aldrich and manganese nitrate (50% w/w solution) was purchased from Sinopharm Chemical Reagent Co. Ltd. Carbon fiber paper (CFP, TGP-H-060, Toray Co. Ltd.) or glass plate served as the substrate materials, which was sequentially cleaned using ultrasonication by acetone, ethanol, and deionized water, followed by hydrophilic treatment (for CFP) by heating on a hot plate at 250 ℃ for 30 min in static air. RuOCl@MnO_x sample was fabricated via one-step heating treatment method as follows. 1 mg $RuCl_3 \cdot xH_2O$ powder and 30 μl 2.15 M $Mn(NO_3)_2$ solution were dissolved in 2 ml deionized water by stirring at room temperature to form mixed precursor solution. Afterward, the solution was dropped slowly onto a 2-cm^2 CFP heated on a hot plate at 210 ℃, then the sample was heated at 210 ℃ for another 10 minutes before being thoroughly rinsed with water. About 46% solution (by comparing mass increments between CFP substrate and underlying quartz spacer after heating deposition) was deposited onto CFP substrate due to its porous structure and hydrophilic surface, corresponding to a loading mass of 0.23 mg cm^{-2} $RuCl_3 \cdot xH_2O$ precursor on CFP. Individual $RuCl_3 \cdot xH_2O$ solution or $Mn(NO_3)_2$ solution dropped on substrate was also prepared using the same heating method to obtain CFP-loaded RuOCl or MnO_x control sample, respectively. RuOCl/MnO_x serving as another control sample was also fabricated by dropwise adding $RuCl_3 \cdot xH_2O$ solution onto as-prepared CFP-loaded MnO_x sample following the same heating procedure.

For the commercial RuO_2 catalyst sample, 4 mg RuO_2 was added to 1 ml of water/ethanol (3:1, v/v) containing 20 μl Nafion solution (5%, DuPont D520), and dispersed by sonication for 1 h to generate homogenous ink. Then 38 μL ink was dropped into 1 cm^2 CFP (by sealing a 2-cm^2 CFP with silicone rubber to define the area) substrate to reach a RuO_2 loading mass of 0.15 mg (denoted as RuO_2|0.15@CFP), which corresponds to the same Ru atomic mass as that in RuOCl@MnO_x, and dropping-drying cycles gave higher loading mass denoted as RuO_2|x@CFP (x=0.15, 0.3, 0.45, 0.6, 0.75, 0.9, 1.05). In addition, 0.15 mg (38 μL) RuO_2 was dropped to as-synthesized CFP-loaded MnO_x (by sealing a 2-cm^2 MnO_x-coated CFP with silicone rubber to define the area to 1 cm^2) to donate RuO_2/MnO_x working electrode.

1.2 Structural characterizations

The morphologies were characterized via field-emission scanning electron microscopy (Hitachi, S-4800; FEI QUANTA 250 FEG; Hitachi, Regulus 8230) and transmission electron microscopy (Themo Fisher, Talos F200x; JEM-ARM200P). Energy dispersive X-Ray spectrometry (EDS) analyses were conducted by the TEM equipment (Talos F200x) equipped with a four quadrant FEI Super-X detector, and by FEI QUANTA 250 FEG SEM equipment. Electron energy loss spectroscopy (EELS) measurement was carried out by another transmission electron microscopy (FEI Tecnai F20). Crystal structure information was investigated by X-ray diffraction (XRD; Bruker D8 Advance Davinci) using Cu Kα ($\lambda = 1.5406$ Å) radiation. Raman spectra were collected via a Renishaw in Via reflex spectrometer at an excitation wavelength of 532 nm. X-ray photoelectron spectroscopy (XPS) study was conducted with a Kratos AXIS SUPPA and a Thermo VG Scientific Escalab 250 system. The concentrations of ions were measured by inductively coupled plasma optical emission spectrometry (ICP-OES, SPECTRO ARCOSII). X-ray absorption spectroscopy (XAS) of samples were collected with the fluorescence mode at beamline station (TPS 44A) in National Synchrotron Radiation Research Center (NSRRC) in Hsinchu, Taiwan. Several metal foils were used for the photon energy calibration.

1.3 Electrochemical measurements

Electrochemical performance tests were carried out on an electrochemical workstation (CHI 660E) with a standard three-electrode setup in an electrolyte of 0.5 M H_2SO_4 after purging with O_2. CFP loaded RuOCl@MnO_x, RuOCl, MnO_x, RuOCl/MnO_x, RuO_2/MnO_x, and RuO_2|x@CFP samples were used as the working electrodes. An Ag/AgCl (saturated KCl) electrode and a Pt wire were used as the reference electrode and counter electrode, respectively. All LSV (linear sweep voltammetry) curves were recorded with the potential sweep rate at 5 mV s^{-1}, and chronopotentiometric measurements were performed at 10 mA cm^{-2}, 100 mA cm^{-2}, 300 mA cm^{-2}, and 500 mA cm^{-2}, respectively. The geometric areas used for electrochemical LSV testing, 10 and 100 mA cm^{-2} chronopotentiometric measurements were 1 cm^2 (by sealing a 2-cm^2 catalyst-coated CFP with silicone rubber to define the area), and the areas used for 300 and 500 mA cm^{-2} chronopotentiometric measurements were 0.5 cm^2. Test areas of LSV curves extended to high anodic potential for CFP-loaded RuO_2|0.15@CFP, RuOCl@MnO_x and MnO_x were 1, 0.5 and 0.5 cm^2, respectively, and the potential scan rate was 0.1 mV s^{-1}. All potentials, with full iR correction (manual iR compensation, where R_s was obtained from EIS result under open-circuit voltage) if not mentioned separately, were converted to a reversible hydrogen electrode (RHE) scale, *i.e.*, E(RHE)=E(Ag/AgCl) + 0.197 V+ 0.059×pH.

1.4 Density Functional Theory (DFT) simulations

In the calculations, bulk RuO_2 (space group: 136, Cell: 8.984 Å×8.984×6.213 Å, α=β=γ=90º), and Mn_2O_3 (space group: 205, Cell: 9.416 Å×9.423 Å×9.405 Å, α=β=γ=90º) were used based on the experimental results. RuO_2 (110) and Mn_2O_3 (110) with a vacuum region of 15 Å were built to simulate the surface reactions. CASTEP module of the Materials Studio software (Accelrys Inc.) was employed for the quantum chemistry calculations. Self-consistent periodic DFT was adopted to explore the electronic structure and catalytic activities. Perdew-Burke-Ernzerhof (PBE) approximation was selected as the Generalized Gradient Approximation (GGA) method to calculate the exchange-correlation energy. The Broyden-Fletcher-Goldfarb-Shanno (BFGS) scheme was selected as the minimization algorithm. Elexreonic minimizer was performed by using an all-bands method that allows simultaneous update of all wavefunctions. And ionic cores were represented by an ultrasoft pseudopotential in reciprocal space. The energy cutoff was 340 eV and the SCF tolerance was 1.0×10^{-6} eV/atom. And the k-points were set as 2×2×2 for bulk Mn_2O_3 and RuO_2, 2×2×1 for RuO_2 (110), and 2×1×1 for Mn_2O_3 (110) surfaces.

The coordination number of Ru is determined based on bond length tolerance from 0.6 to 1.1 by Calculate Bonds tool. The Calculate Bonds tool creates bonds between two atoms if the following criteria are met: (1) neither of the two atoms is excluded from forming bonds, *i.e.*, they are not elements in the element exclusion list, and (2) the sum of the covalent radii of the two atoms fulfills the bond-length criterion, *i.e.*, $TolFac_{lower}$ × ideal distance < distance < $TolFac_{upper}$ × ideal distance, where distance = distance between the two atoms forming the bond. $TolFac_{lower}$, the lower tolerance factor, determines the smallest distance between two atoms for which a bond may still be formed. The distance between the atoms has to be at least the ideal bond length times this value. $TolFac_{upper}$, upper tolerance factor, determines the largest distance between two atoms for which a bond may still be formed. The distance between the atoms has to be smaller than the ideal bond length times this value. Ideal distance = R_{cov}(Atom1) + R_{cov}(Atom2), where R_{cov} denotes the covalent radius of the atom.

The optimization was completed when the energy, maximum force, maximum stress, and maximum displacement were smaller than 1.0×10^{-5} eV/atom, 0.03 eV/ Å, 0.05 GPa, and 0.001 Å, respectively. The Gibbs free energy during OER process was calculated based on four-electron-transfer process, and detailed calculation can be found in the previous publication [Hu, J., et al. ACS Appl. Mater. Interfaces 10, 5475-5484 (2018)]. The solvation effect was not taken into account in the calculation of the adsorption energies of species. The surface energy (E_{sur}) and formation energy (E_{form}) were calculated by the following eq. (1) and (2):

$$E_{sur} = \frac{1}{2A}(E_{surface} - nE_{bulk}) \quad (1)$$

$$E_{form} = \frac{1}{n_M + n_O}(nE_{bulk} - n_M E_M - n_O E_O) \quad (2)$$

where E_{bulk} is the total energy per unit cell of the bulk, n is the number of unit cells that the slab model contains, and A is the surface area of the slab model. E_M is the bulk energy of per metal atom. E_O is half of oxygen energy. n_M and n_O are the number of metal and oxygen atom in bulk system, respectively.

2. Supplementary Results

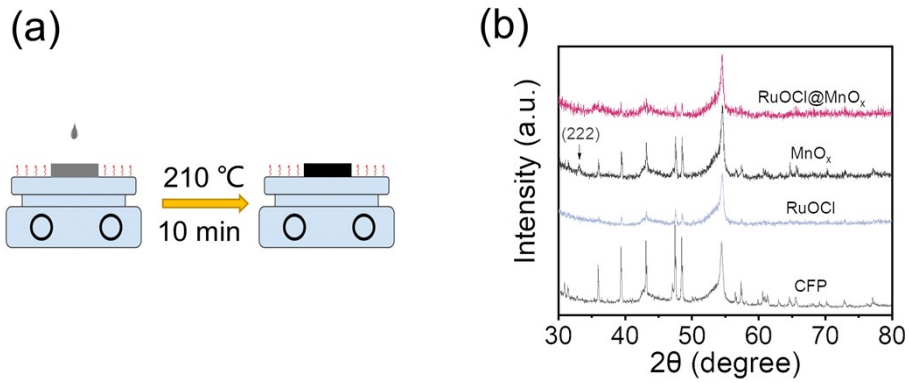

Fig. S1 (a) Schematic illustration of the material fabrication procedure. (b) XRD pattern of CFP-loaded RuOCl@MnO_x, MnO_x, RuOCl, and CFP.

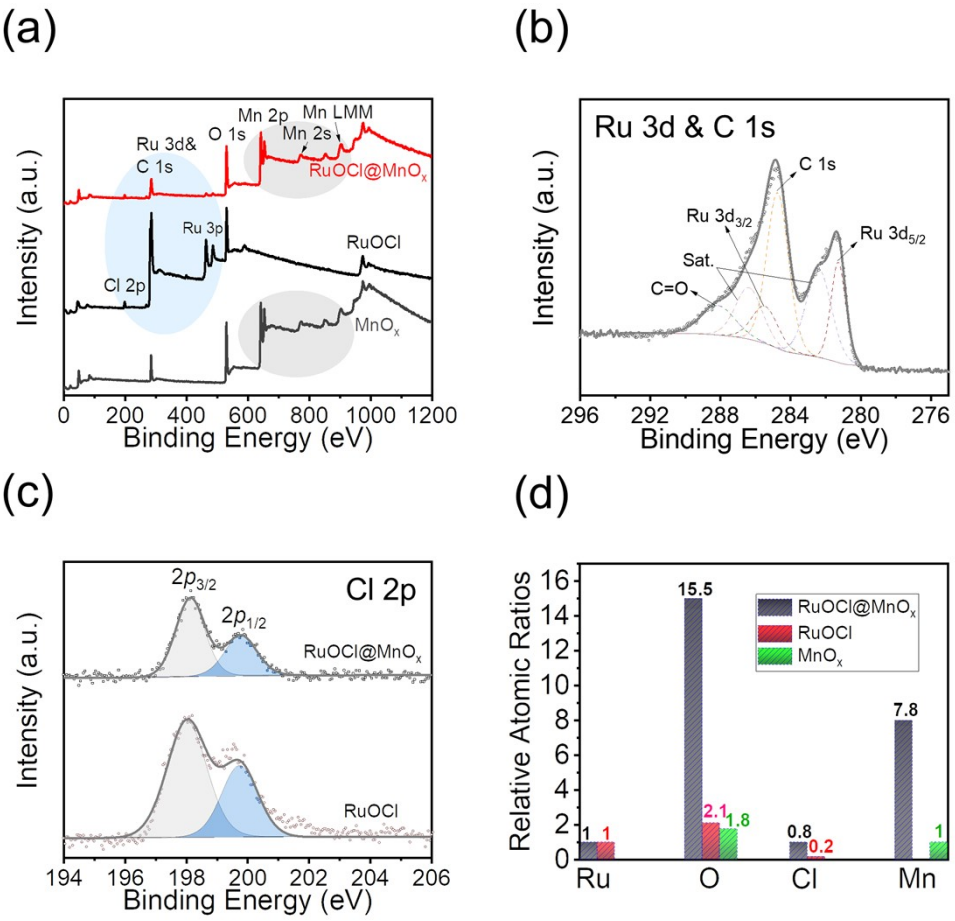

Fig. S2 (a) XPS full spectra of RuOCl@MnO_x, RuOCl, and MnO_x. (b) Ru 3d/C 1s XPS profiles of RuOCl@MnO_x. Sat. represents the satellite peaks of Ru 3d [Tian, Y., *et al. iScience* 23, 100756 (2020)]. (c) XPS spectra of Cl 2p of RuOCl@MnO_x and RuOCl. (d) The atomic ratios obtained from XPS results, where the atomic concentrations are normalized to that of Ru in RuOCl@MnO_x and RuOCl samples, and to that of Mn in MnO_x.

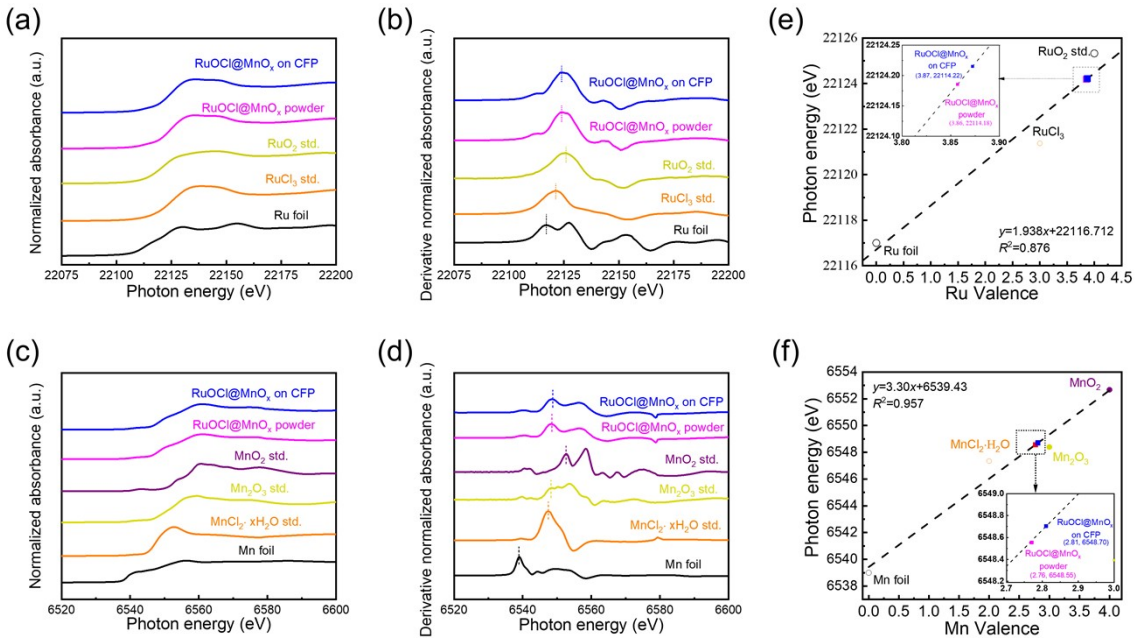

Fig. S3 Ru K-edge (a-b) and Mn K-edge (c-d) normalized XANES and derivative normalized XANES spectra. Standard-driven linear regression for Ru (e) and Mn (f) samples.

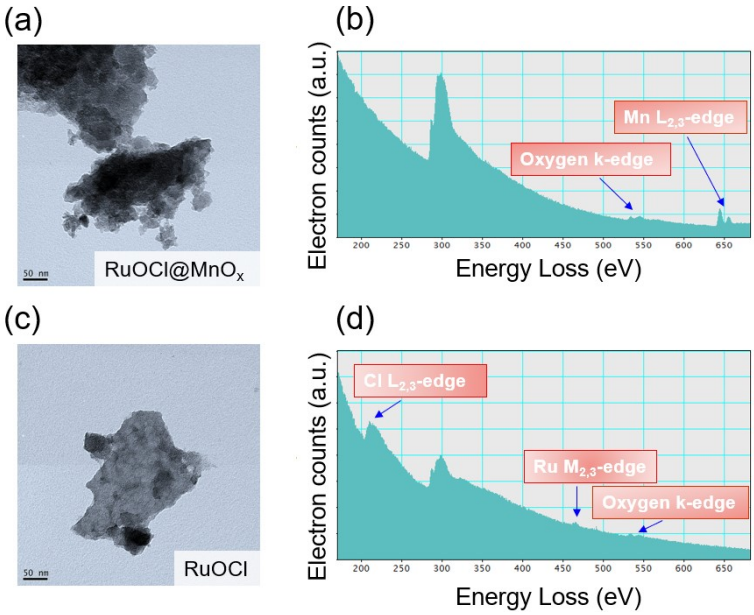

Fig. S4 TEM images of (a) RuOCl@MnO_x and (c) RuOCl, and electron energy loss spectroscopy (EELS) pattern of (b) RuOCl@MnO_x and (d) RuOCl samples.

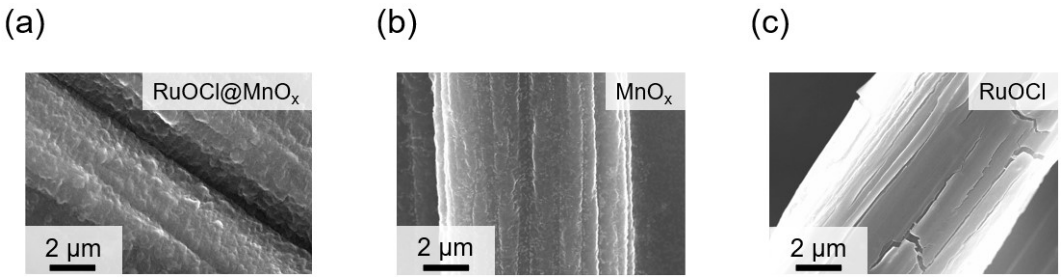

Fig. S5 SEM images of (a) RuOCl@MnO_x, (b) MnO_x, and (c) RuOCl.

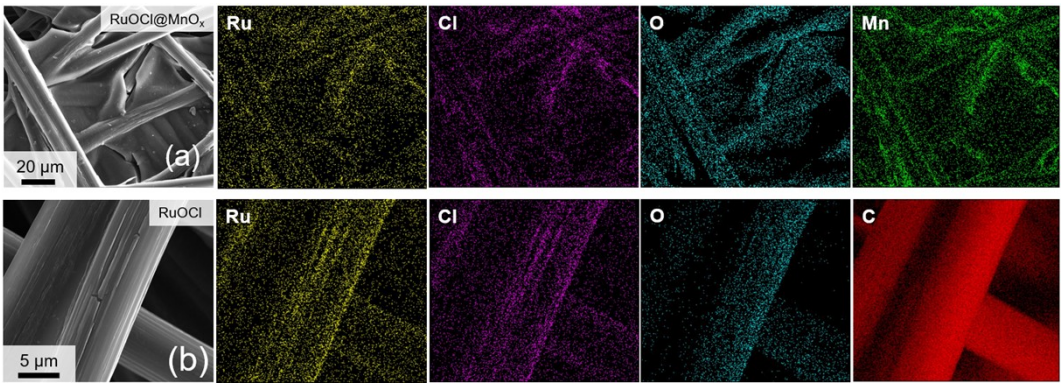

Fig. S6 SEM-EDS (Energy Dispersive Spectrometer) images of RuOCl@MnO_x and RuOCl samples. The elemental mapping region is (a) and (b), and Ru L_α, Cl K_α, O K_α, Mn K_α, C K_α SEM-EDS mappings are displayed.

(a)

ions	Ru / mg L^{-1}	Mn / mg L^{-1}
	0.419	2.192

(b)

Ions dissolved in electrolyte	Working electrode area	Ru / mg L^{-1}	Mn / mg L^{-1}
10 mA cm^{-2} for 280 h	1 cm^2	1.405	1.502
100 mA cm^{-2} for 200 h	1 cm^2	1.469	1.685
300 mA cm^{-2} for 100 h	0.5 cm^2	0.857	0.982
500 mA cm^{-2} for 50 h	0.5 cm^2	1.004	1.275

(c)

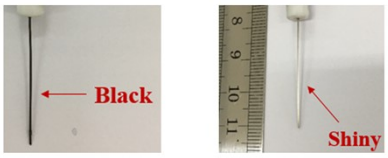

Fig. S7 (a) ICP-OES results of the prepared RuOCl@MnO_x. A piece of CFP-loaded RuOCl@MnO_x (1 cm^2) was placed into 10 mL concentrated hydrochloric acid at 60 ℃ for 20 min, and then the solution was transferred to a 250-mL volumetric flask for quantification with 0.23 mol L^{-1} HNO_3. The blank sample with pure CFP was subjected to the same treatment. (b) ICP-OES results of the electrolytes (50 mL) after 280-h, 200-h, 100-h, and 50-h chronopotentiometry tests at 10, 100, 300, and 500 mA cm^{-2}, respectively. The acidity was adjusted with 0.23 M nitric acid and the ionic concentration has been converted to be similar to that dissolved in the original electrolyte. The blank sample was subjected to the same treatment, except that no chronopotentiometry test was performed. (c) Deposition of Ru on cathodic Pt wire was observed after long-term test (left panel), and the Ru was returned to solution by applying a high voltage (2 V) for a short time (30 s) to obtain a shiny Pt wire (right panel) and more accurate ion concentrations. Notably, the Ru deposited on the cathode Pt has no significant effect on the anodic OER process studied here.

	RuOCl@MnO_x				MnO_x		RuOCl		
Atomic ratio	Ru	Mn	O	Cl	Mn	O	Ru	O	Cl
XPS	1	7.8	15.5	0.8	1	1.8	1	2.1	0.2
EDS	1	11.1	18.0	1.6	1	1.7	1	2.4	0.4
ICP-OES	1	9.6							

Table S1. A summary of atomic ratios obtained from XPS/EDS/ICP-OES, where the atomic concentrations are normalized to that of Ru in RuOCl@MnO_x and RuOCl samples, and to that of Mn in MnO_x.

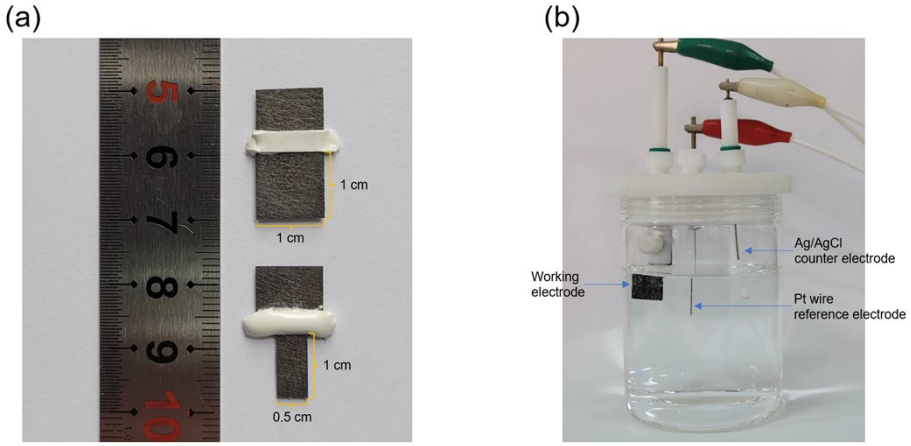

Fig. S8 Photographs of (a) prepared carbon fiber paper electrodes coated with RuOCl@MnO_x, where silicone rubber isolates the testing area of 1 cm^2 (upper) or 0.5 cm^2 (lower), and (b) a three-electrode setup for OER chronopotentiometric measurement at 10 mA cm^{-2} in 0.5 M H_2SO_4.

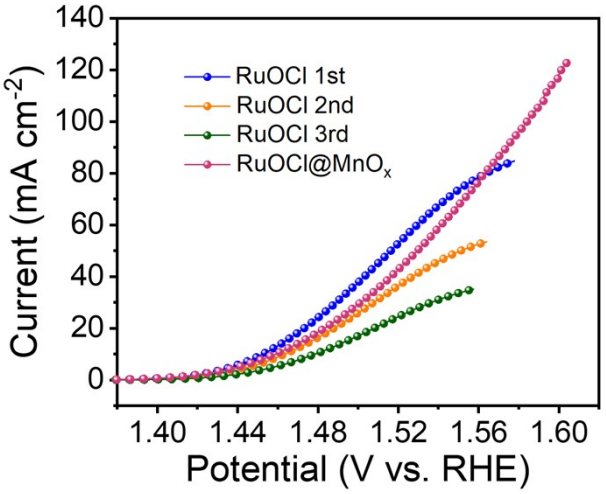

Fig. S9 LSV curves of RuOCl for the first, second, and third tests, and the LSV curve of RuOCl@MnO_x.

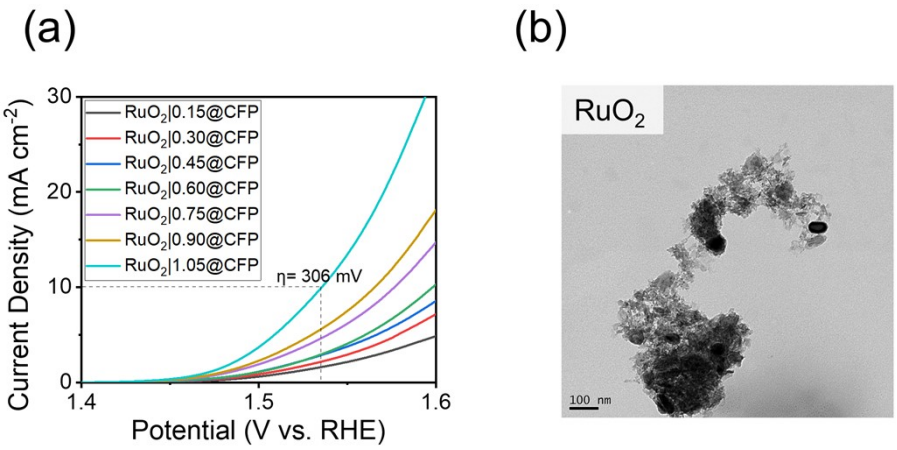

Fig. S10 (a) LSV curves of RuO_2|x@CFP (x=0.15, 0.3, 0.45, 0.6, 0.75, 0.9, 1.05). (b) TEM image of commercially purchased RuO_2.

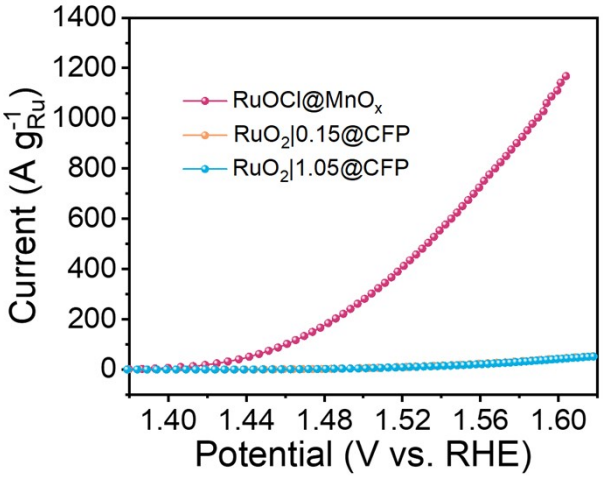

Fig. S11 Mass activity of RuOCl@MnO_x, RuO_2|0.15@CFP, and RuO_2|1.05@CFP.

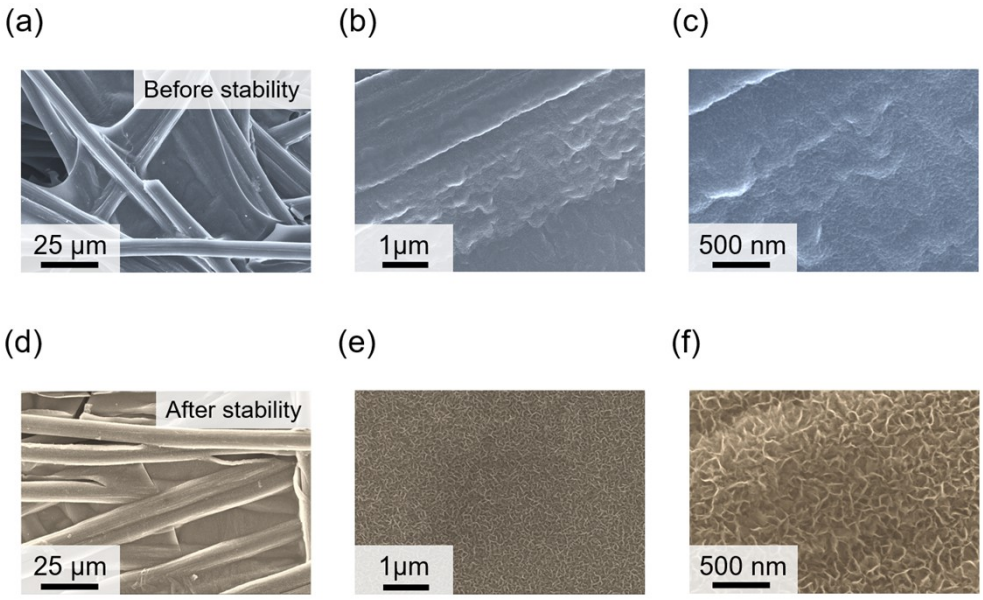

Fig. S12 SEM images of RuOCl@MnO_x before (a-c) and after (d-f) 280-h stability test with enlarged magnification from left to right.

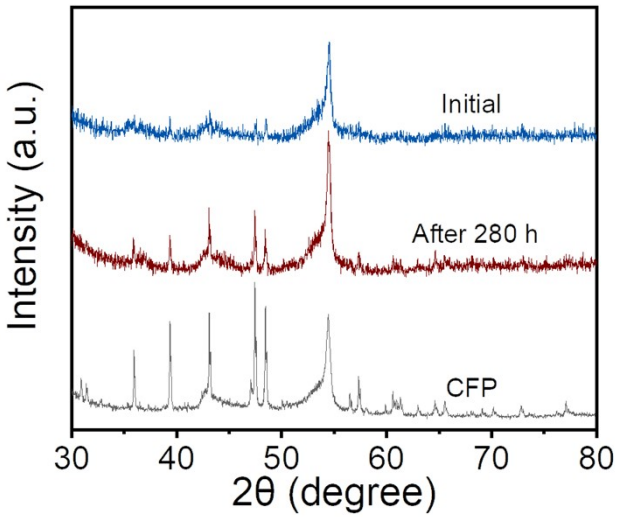

Fig. S13 XRD pattern of initial RuOCl@MnO_x, and that after 280-h stability test, and carbon fiber paper (CFP).

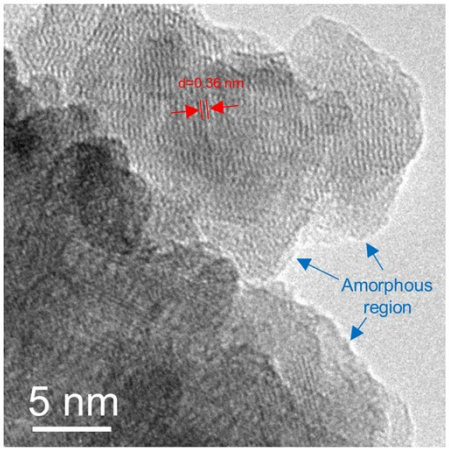

Fig. S14 HRTEM image of RuOCl@MnO_x after 280-h stability test at 10 mA cm^{-2}.

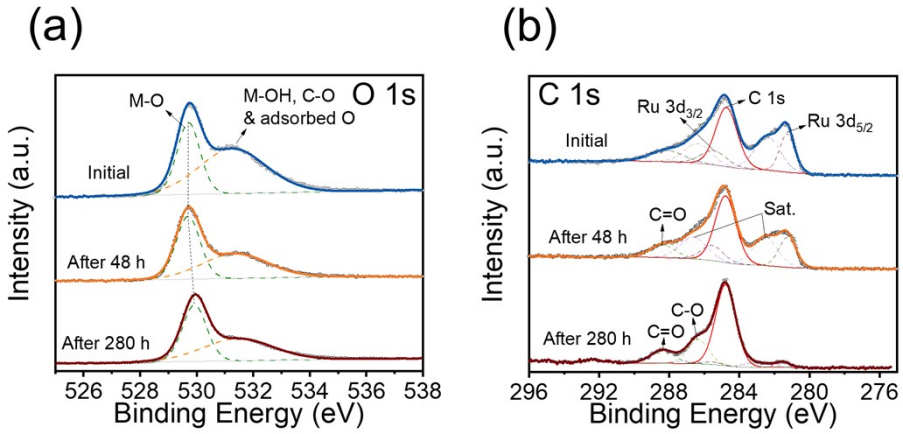

Fig. S15 XPS spectra of (a) O 1s and (b) C 1s/Ru 3d states of initial RuOCl@MnO_x, and that after 48-h stability test, after 280-h stability test at 10 mA cm^{-2}. The C 1s peaks have been corrected to 284.8 eV.

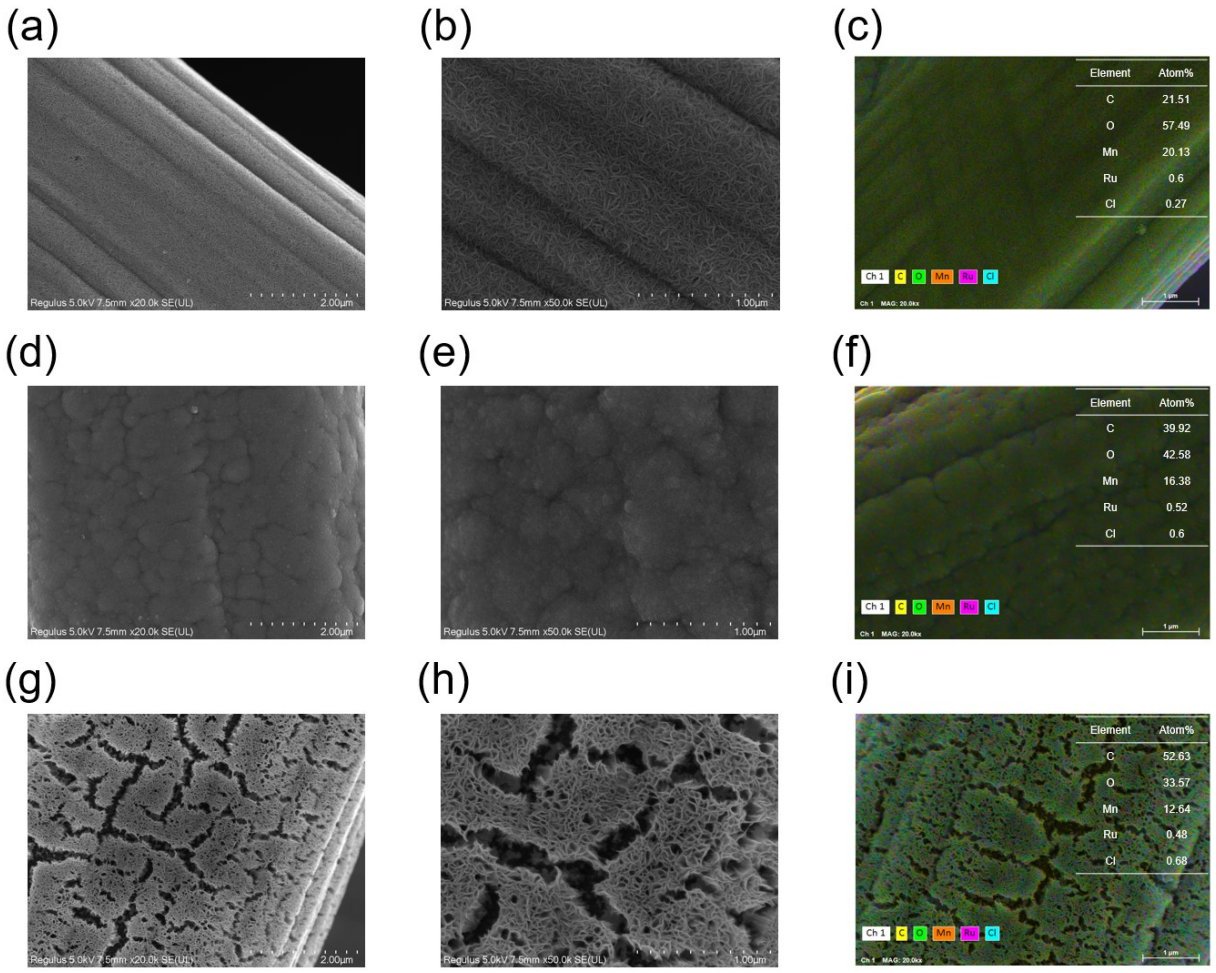

Fig. S16 SEM images and SEM-EDS full element mappings with atomic ratios of RuOCl@MnO_x after (a-c) 200-h stability test at 100 mA cm^{-2}, (d-f) 100-h stability test at 300 mA cm^{-2}, (g-i) 50-h stability test at 500 mA cm^{-2}.

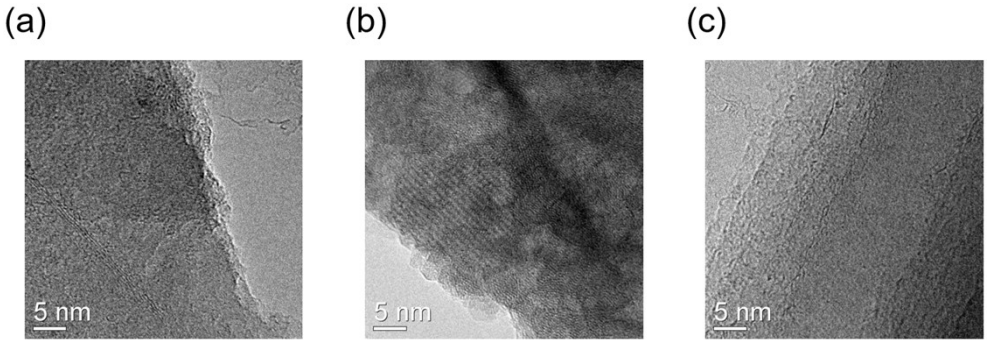

Fig. S17 HRTEM image of RuOCl@MnO_x after (a) 200-h stability test at 100 mA cm^{-2}, (b) 100-h stability test at 300 mA cm^{-2}, (c) 50-h stability test at 500 mA cm^{-2}.

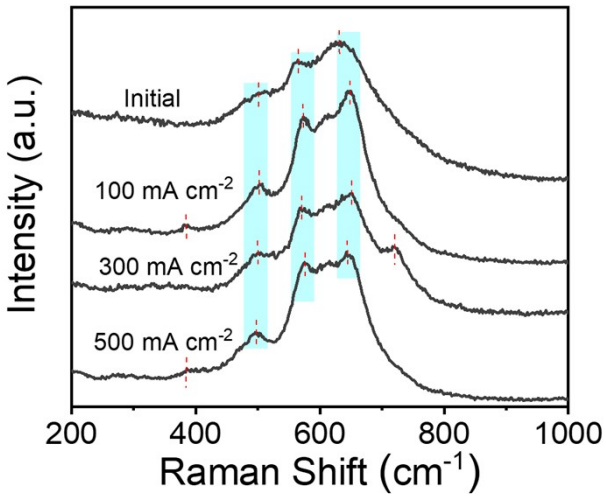

Fig. S18 Raman spectra of initial RuOCl@MnO_x, and that after 200-h stability test at 100 mA cm^{-2}, after 100-h stability test at 300 mA cm^{-2}, and after 50-h stability test at 500 mA cm^{-2}.

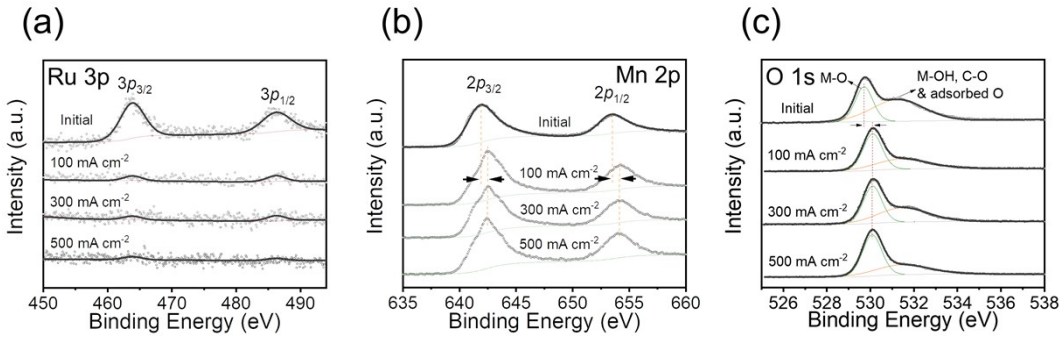

Fig. S19 XPS spectra of (a) Ru 3p, (b) Mn 2p, and (c) O 1s states of initial RuOCl@MnO_x, and that after 200-h stability test at 100 mA cm^{-2}, after 100-h stability test at 300 mA cm^{-2}, and after 50-h stability test at 500 mA cm^{-2}.

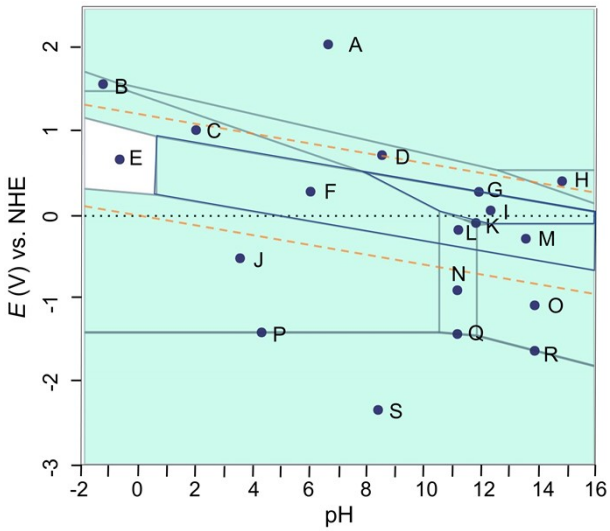

Fig. S20 The Pourbaix diagram of 89-11% Mn-Ru system in aqueous solution based on the reported method [Toma, F. M., *et al. Nat. Commun.* 7, 12012 (2016)], assuming Mn and Ru ion concentration at 10^{-8} mol.kg^{-1}. RuO_4(aq) is appropriate here to describe the state of Ru at high positive potentials [Lin, C., *et al. J. Electrochem. Soc.* 166, D476 (2019); Cui, H., *et al. J. Electrochem. Soc.* 159, H335 (2012); Juodkazytė, J., *et al. Trans. IMF* 85, 194-201 (2007)]. Regions are labelled for stable phases of: A-MnO_4^-+RuO_4(aq); B-Mn^{3+}+RuO_4(aq); C-Mn^{2+}+RuO_4(aq); D-MnO_2(s)+RuO_4(aq); E-Mn^{2+}+$Ru(OH)_2^{2+}$; F-Mn^{2+}+RuO_2(s); G-Mn_2O_3(s)+RuO_4(aq); H-MnO_4^{2-}+RuO_4(aq); I-Mn_2O_3(s)+RuO_2(s); J-Mn^{2+}+Ru(s); K-Mn_3O_4(s)+RuO_2(s); L-$MnOH^+$+RuO_2(s); M-$Mn(OH)_3^-$+RuO_2(s); N-$MnOH^+$+Ru(s); O-$Mn(OH)_3^-$+Ru(s); P-Mn^{2+}+$MnRu_3$(s); Q-$MnOH^+$+$MnRu_3$(s); R-$Mn(OH)_3^-$+$MnRu_3$(s); S-Mn(s)+$MnRu_3$(s).

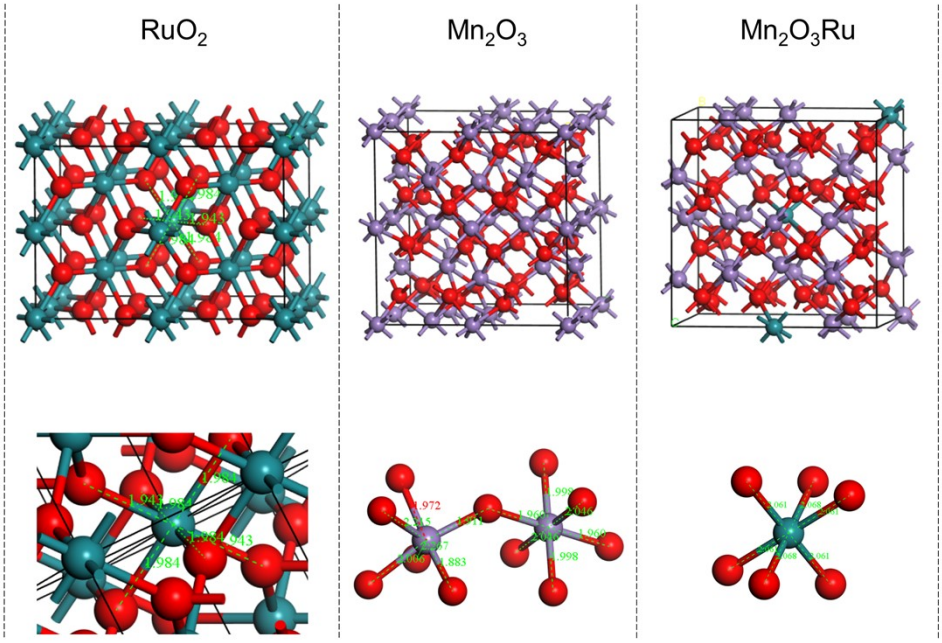

Fig. S21 Established simulation models in bulk forms, and calculated bond lengths after structural optimization of RuO_2, Mn_2O_3, and Mn_2O_3Ru, where Ru, O, and Mn atoms are shown with green, red, and purple spheres, respectively.

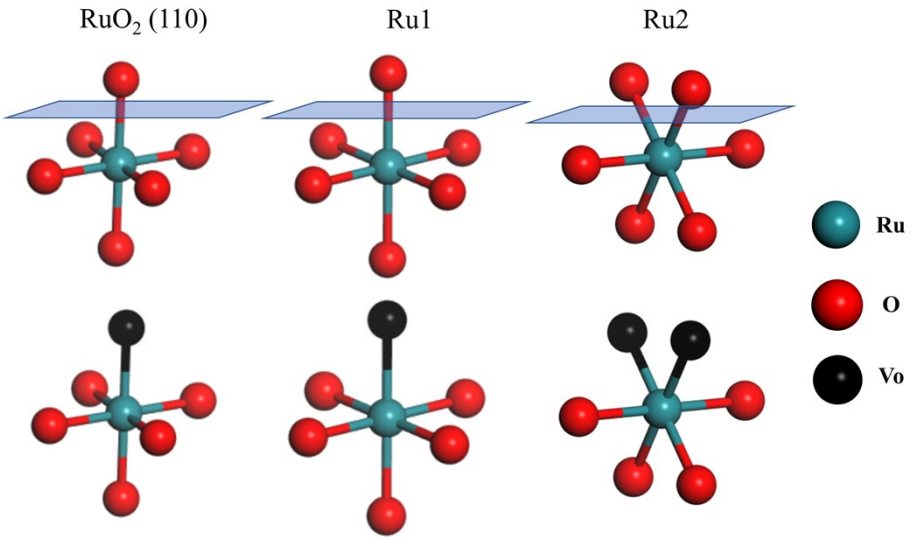

Fig. S22 Comparison of structure units on the (110) surface without vacancy defects (upper) and with vacancy defects (lower) of RuO_2, Ru1 in Mn_2O_3Ru, and Ru2 in Mn_2O_3Ru.

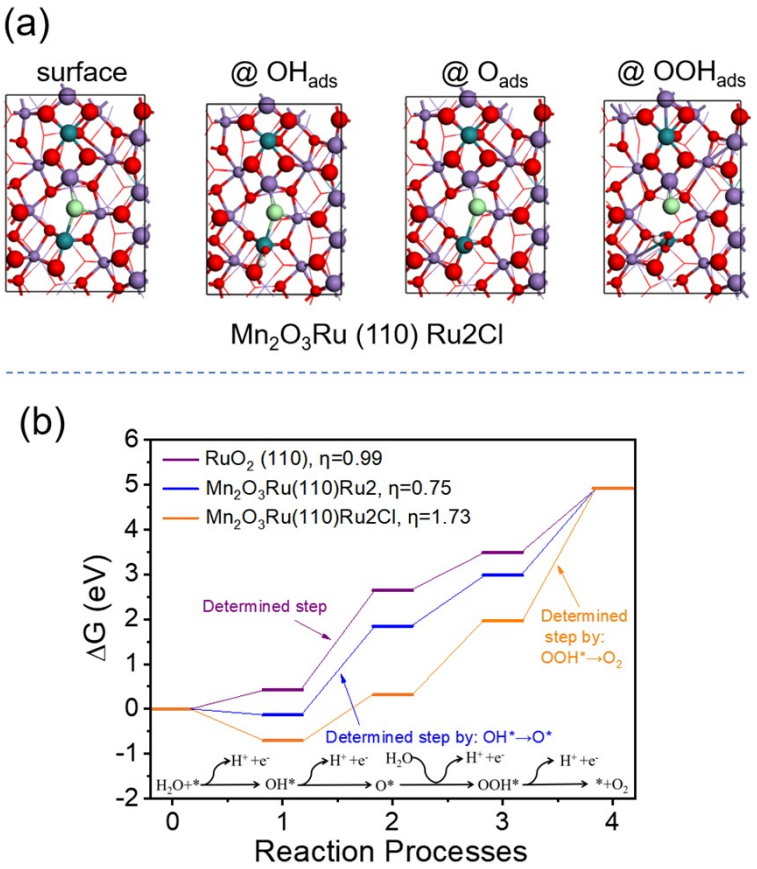

Fig. S23 (a) The geometric structures as well as the OER intermediates of Mn_2O_3Ru (110) Ru2Cl, where Ru (dark green), Mn (purple), O (red), Cl (light green), and H (white) atoms are shown in colored spheres. (b) Free-energy profiles of OER.

OER catalysts	Electrolyte	Mass activity	Stability	Overpotential (mV vs. RHE) @ 10 mA cm^{-2}	Tafel slope (mV dec^{-1})	Ref.
$RuOCl@MnO_x$	0.5 M H_2SO_4	481 A g_{Ru}^{-1}@η=300 mV 288 A g_{Ru}^{-1}@η=270 mV	**280 h@10 mA cm^{-2}; 200 h@100 mA cm^{-2}**	228	43	This work
$Y_2Ru_2O_{7-\delta}$	0.1 M $HClO_4$	213 A g_{Ru}^{-1}@η=270 mV	8 h@1 mA cm^{-2}	N/A	55	[1]
Co-RuIr	0.1 M $HClO_4$	N/A	25 h@10 mA cm^{-2}	235	66.9	[2]
MS-IrO_2/RuO_2	0.1 M $HClO_4$	~129 A g_{Ru+Ir}^{-1} @η=300 mV	22 mV decay after 2h@10 mA cm^{-2}	300	121	[3]
RuRh@(RuRh)O_2	0.1 M $HClO_4$	~485 A g_{Ru+Rh}^{-1} @η=300 mV	~120 mV decay after 2h @5 mA cm^{-2}	245	51.2	[4]
$Y_{1.8}Cu_{0.2}Ru_2O_{7-\delta}$	1 N H_2SO_4	~60 A g_{Ru}^{-1}@η=270 mV	6h@1 mA cm^{-2}	~360	52	[5]
$Ni_{0.04}Co_{0.06}Ru_{0.9}O_2$	0.1 M $HClO_4$	~240 A g_{Ru}^{-1} @η=470 mV	35% decay after 5h@1.7 V	~320	32	[6]
$Cr_{0.6}Ru_{0.4}O_2$	0.5 M H_2SO_4	229 A g_{Ru}^{-1}@η=270 mV	10 h@10 mA cm^{-2}	178	56	[7]
Ruthenate nanosheets from $NaRuO_2$	0.1 M $HClO_4$	~161 A g_{Ru}^{-1} @η=300 mV	260 mV decay after 6h @10 mA cm^{-2}	255	38	[8]
$IrRuO_x/TiO_2$	0.5 M H_2SO_4	80 A g_{Ru+Ir}^{-1}@η=320 mV	10% decay after 100 CV cycles@1-1.63 V	~320	71	[9]
1×$RuO_2@C@SiO_2$	3 M H_2SO_4	~76 A g_{Ru}^{-1}@η=330 mV	77 mV decay after 24h@10 mA cm^{-2}	282	N/A	[10]
$Pt_{39}Ir_{10}Pd_{11}$	0.1 M $HClO_4$	200 A $g_{Ir+Pt+Pd}^{-1}$ @η=300 mV	N/A	372	128.7	[11]
Sr_2NiIrO_6	0.1 M $HClO_4$	115 A g_{Ir}^{-1}@η=295 mV	1 h@10 mA cm^{-2}	295	48	[12]
IrO_2 Nanoneedle	1 M H_2SO_4	60 A g_{Ir}^{-1}@η=320 mV	2 h@10 mA cm^{-2}	313	57	[13]
Ir black or Ir/C	0.05 M H_2SO_4	8.0 or 31.1 A g_{Ir}^{-1} @η=280 mV	deactivation after 6 or 10 h @1 mA cm^{-2}	~495 or ~450	56.8 or 55.6	[14]
Ir-ND/ATO	0.05 M H_2SO_4	69.8 A g_{Ir}^{-1}@η=280 mV	15 h@ 1 mA cm^{-2}	~400	56.4	[14]
$Pr_2Ir_2O_7$	0.1 M $HClO_4$	424.5 A g_{Ir}^{-1}@η=300 mV	2.8 h@10 mA cm^{-2}	295	N/A	[15]
IrOOH nanosheets	0.1 M $HClO_4$	10.5 A g_{Ir}^{-1}@η=300 mV	150 mV decay after 7 h @10 mA cm^{-2}	344	58	[16]
$IrNiO_x$	0.05 M H_2SO_4	~175 A g_{Ir}^{-1}@η=270 mV	75 oxidation cycles	N/A	N/A	[17]
P-$IrCu_{1.4}$ NCs	0.05 M H_2SO_4	~213 A g_{Ir}^{-1}@η=320 mV	10 h@10 mA cm^{-2}	311	53.9	[18]
$Bi_2Ir_2O_7$	0.1 M $HClO_4$	26 A g_{Ir}^{-1}@η=295 mV	500 potential step cycles@1.6 V	N/A	45	[19]
Ba_2PrIrO_6	0.1 M $HClO_4$	244 A g_{Ir}^{-1}@η=300 mV	1 h@10 mA cm^{-2}	390	60	[20]
IrO_2-TiO_2	0.1 M $HClO_4$	70 A g_{Ir}^{-1}@η=295 mV	10% decrease after 100 cycles @1.6 V	N/A	42	[21]
$W_{0.57}Ir_{0.43}O_{3-\sigma}$	1 M H_2SO_4	33 A g_{Ir}^{-1}@η=370 mV	0.6 h@1 mA cm^{-2}	370±2	125	[22]
Co-doped $SrIrO_3$(6H)	0.1 M $HClO_4$	140 A g_{Ir}^{-1}@η=295 mV	20 h@1 mA cm^{-2}	235±5	51.8	[23]
H-Ti@IrO_x	0.5 M H_2SO_4	1500 A g_{Ir}^{-1}@η=350 mV	130 h@200 mA cm^{-2}	277	29	[24]

IrRu@Te	0.5 M H_2SO_4	590 A g_{IrRu}^{-1}@η=270 mV	20 h@10 mA cm^{-2}	220	35	[25]
RuIr@CoNC	0.5 M H_2SO_4	2041 A g_{RuIr}^{-1}@η=300 mV	40 h@10 mA cm^{-2}	223	45	[26]

Table S2. Comparison of the performance of Ru- and Ir-based electrocatalysts for the OER under acidic media. Note: the data with "~" are extracted from the related figures or calculated from given data in articles.

Supplementary Note 1:

To assess the worst-case scenario, we assume both Ru ($Ru^{4+}\rightarrow Ru^{8+}$) and Mn ($Mn^{3+}\rightarrow Mn^{7+}$) in the catalyst are completely oxidized to the highest valence state at the anode. To determine the Coulomb ratio, the loading masses of Ru and Mn are obtained from inductively coupled plasma optical emission spectroscopy (ICP-OES) measurement results.

The oxidation charges of ruthenium and manganese are thus:

(0.105×10^{-3}) g÷101.1 g/mol×4e$^-$×$(1.6\times10^{-19}$ C/e$^-$)×$(6.02\times10^{23}$ /mol)=0.4 C

(0.548×10^{-3}) g÷54.94 g/mol×4e$^-$×$(1.6\times10^{-19}$ C/e$^-$)×$(6.02\times10^{23}$ /mol)=3.8 C

The ratios of the charges of ruthenium and manganese oxidized to the highest valence state to the OER charge at the four current (0.01, 0.1, 0.15, and 0.25 A) are:

4.2 C÷(0.01 A×280 h×3600 s/h)×100%=4.2×10^{-4}

4.2 C÷(0.1 A×200 h×3600 s/h)×100%=5.8×10^{-5}

4.2 C÷(0.15 A×100 h×3600 s/h)×100%=7.8×10^{-5}

4.2 C÷(0.25 A×50 h×3600 s/h)×100%=9.3×10^{-5}

For the cathode, the HER charge is the same as the anodic OER charge. Similarly, assuming the worst-case scenario of extreme metal reduction $Ru^{8+}\rightarrow Ru^0$ and $Mn^{7+}\rightarrow Mn^0$, the ratios of the charges of ruthenium and manganese reduced to the lowest valence state to the HER charge at the four current (0.01, 0.1, 0.15, and 0.25 A) can be calculated as:

7.5 C÷(0.01 A×280 h×3600 s/h)×100%=7.4×10^{-4}

7.5 C÷(0.1 A×200 h×3600 s/h)×100%=1.0×10^{-4}

7.5 C÷(0.15 A×100 h×3600 s/h)×100%=1.4×10^{-4}

7.5 C÷(0.25 A×50 h×3600 s/h)×100%=1.7×10^{-4}

In actual experiments, the ratio of the charge of Ru and Mn elements oxidized/reduced to the charge of O_2 or H_2 evolution is much smaller than those in the above worst-case scenarios, as suggested by the finite dissolved mass of Ru (0.07 mg) and Mn (0.08 mg), as well as the finite valence state shift (*e.g.*, from Mn^{3+} to the Mn^{4+}) after long-term stability tests. Therefore, the charge involved in redox reactions of the metal elements is negligible with respect to those involved in OER or HER especially at high current density.

Supplementary References

[1] J. Kim, P.-C. Shih, K.-C. Tsao, Y.-T. Pan, X. Yin et al., High-performance pyrochlore-type yttrium ruthenate electrocatalyst for oxygen evolution reaction in acidic media. J. Am.

Chem. Soc. **139**(34), 12076-12083 (2017).

[2] J. Shan, T. Ling, K. Davey, Y. Zheng, S. Z. Qiao. Transition-metal-doped RuIr bifunctional nanocrystals for overall water splitting in acidic environments. Adv. Mater. **31**(17), 1900510 (2019).

[3] S. W. Lee, C. Baik, T.-Y. Kim, C. Pak. Three-dimensional mesoporous Ir-Ru binary oxides with improved activity and stability for water electrolysis. Catal. Today **352**, 39-46 (2020).

[4] K. Wang, B. Huang, W. Zhang, F. Lv, Y. Xing et al., Ultrathin RuRh@(RuRh)O_2 core@shell nanosheets as stable oxygen evolution electrocatalysts. J. Mater. Chem. A **8**(31), 15746-15751 (2020).

[5] D. A. Kuznetsov, M. A. Naeem, P. V. Kumar, P. M. Abdala, A. Fedorov et al., Tailoring lattice oxygen binding in ruthenium pyrochlores to enhance oxygen evolution activity. J. Am. Chem. Soc. **142**(17), 7883-7888 (2020).

[6] Y. Wu, M. Tariq, W. Q. Zaman, W. Sun, Z. Zhou et al., Ni-Co codoped RuO_2 with outstanding oxygen evolution reaction performance. ACS Appl. Energy Mater. **2**(6), 4105-4110 (2019).

[7] Y. Lin, Z. Tian, L. Zhang, J. Ma, Z. Jiang et al., Chromium-ruthenium oxide solid solution electrocatalyst for highly efficient oxygen evolution reaction in acidic media. Nat. Commun. **10**(1), 1-13 (2019).

[8] S. Laha, Y. Lee, F. Podjaski, D. Weber, V. Duppel et al., Ruthenium oxide nanosheets for enhanced oxygen evolution catalysis in acidic medium. Adv. Energy Mater. **9**(15), 1803795 (2019).

[9] A. Martínez-Séptimo, M. Valenzuela, P. Del Angel, R. d. G. González-Huerta. $IrRuO_x/TiO_2$ a stable electrocatalyst for the oxygen evolution reaction in acidic media. Int. J. Hydrogen Energy **46**, 25918-25928 (2021).

[10] P. A. DeSario, C. N. Chervin, E. S. Nelson, M. B. Sassin, D. R. Rolison. Competitive oxygen evolution in acid electrolyte catalyzed at technologically relevant electrodes painted with nanoscale RuO_2. ACS Appl. Mater. Interfaces **9**(3), 2387-2395 (2017).

[11] J. Zhu, M. Xie, Z. Chen, Z. Lyu, M. Chi et al., Pt-Ir-Pd trimetallic nanocages as a dual catalyst for efficient oxygen reduction and evolution reactions in acidic media. Adv. Energy Mater. **10**(16), 1904114 (2020).

[12] M. Retuerto, L. Pascual, O. Piqué, P. Kayser, M. A. Salam et al., How oxidation state and lattice distortion influence the oxygen evolution activity in acid of iridium double perovskites. J. Mater. Chem. A **9**(5), 2980-2990 (2021).

[13] J. Lim, D. Park, S. S. Jeon, C. W. Roh, J. Choi et al., Ultrathin IrO_2 nanoneedles for electrochemical water oxidation. Adv. Funct. Mater. **28**(4), 1704796 (2018).

[14] H.-S. Oh, H. N. Nong, T. Reier, M. Gliech, P. Strasser. Oxide-supported Ir nanodendrites with high activity and durability for the oxygen evolution reaction in acid PEM water electrolyzers. Chem. Sci. **6**(6), 3321-3328 (2015).

[15] C. Shang, C. Cao, D. Yu, Y. Yan, Y. Lin et al., Electron correlations engineer catalytic activity of pyrochlore iridates for acidic water oxidation. Adv. Mater. **31**(6), 1805104 (2019).

[16] D. Weber, L. M. Schoop, D. Wurmbrand, S. Laha, F. Podjaski et al., IrOOH nanosheets as acid stable electrocatalysts for the oxygen evolution reaction. J. Mater. Chem. A **6**(43), 21558-21566 (2018).

[17] H. N. Nong, T. Reier, H.-S. Oh, M. Gliech, P. Paciok et al., A unique oxygen ligand environment facilitates water oxidation in hole-doped $IrNiO_x$ core-shell electrocatalysts. Nat. Catal. **1**(11), 841-851 (2018).

[18] Y. Pi, J. Guo, Q. Shao, X. Huang. Highly efficient acidic oxygen evolution electrocatalysis enabled by porous Ir-Cu nanocrystals with three-dimensional electrocatalytic surfaces. Chem. Mater. **30**(23), 8571-8578 (2018).

[19] D. Lebedev, M. Povia, K. Waltar, P. M. Abdala, I. E. Castelli et al., Highly active and stable iridium pyrochlores for oxygen evolution reaction. Chem. Mater. **29**(12), 5182-5191 (2017).

[20] O. Diaz-Morales, S. Raaijman, R. Kortlever, P. J. Kooyman, T. Wezendonk et al., Iridium-based double perovskites for efficient water oxidation in acid media. Nat. Commun. **7**(1), 1-6 (2016).

[21] E. Oakton, D. Lebedev, M. Povia, D. F. Abbott, E. Fabbri et al., IrO_2-TiO_2: A high-surface-area, active, and stable electrocatalyst for the oxygen evolution reaction. ACS Catal. **7**(4), 2346-2352 (2017).

[22] S. Kumari, B. P. Ajayi, B. Kumar, J. B. Jasinski, M. K. Sunkara et al., A low-noble-metal $W_{1-x}Ir_xO_{3-\delta}$ water oxidation electrocatalyst for acidic media via rapid plasma synthesis. Energy Environ. Sci. **10**(11), 2432-2440 (2017).

[23] L. Yang, H. Chen, L. Shi, X. Li, X. Chu et al., Enhanced iridium mass activity of 6H-phase, Ir-based perovskite with nonprecious incorporation for acidic oxygen evolution electrocatalysis. ACS Appl. Mater. Interfaces **11**(45), 42006-42013 (2019).

[24] Z. Yu, J. Xu, Y. Li, B. Wei, N. Zhang et al., Ultrafine oxygen-defective iridium oxide nanoclusters for efficient and durable water oxidation at high current densities in acidic

media. J. Mater. Chem. A **8**(46), 24743-24751 (2020).

[25] J. Xu, Z. Lian, B. Wei, Y. Li, O. Bondarchuk et al., Strong electronic coupling between ultrafine iridium-ruthenium nanoclusters and conductive, acid-stable tellurium nanoparticle support for efficient and durable oxygen evolution in acidic and neutral media. ACS Catal. **10**(6), 3571-3579 (2020).

[26] J. Xu, J. Li, Z. Lian, A. Araujo, Y. Li et al., Atomic-step enriched ruthenium-iridium nanocrystals anchored homogeneously on MOF-derived support for efficient and stable oxygen evolution in acidic and neutral media. ACS Catal. **11**(6), 3402-3413 (2021).